Journal of Solid State Chemistry **163,** 484–490 (2002)
doi:10.1006/jssc.2001.9433, available online at http://www.idealibrary.com on IDEAL®

Phase Diagram and Phase Transitions in the Relaxor Ferroelectric $Pb(Fe_{2/3}W_{1/3})O_3$–$PbTiO_3$ System

L. Feng and Z.-G. Ye[1]

Department of Chemistry, Simon Fraser University, 8888 University Drive, Burnaby, BC, V5A 1S6, Canada

Received February 28, 2001; in revised form August 28, 2001; accepted October 26, 2001

A complete solid solution between relaxor ferroelectric $Pb(Fe_{2/3}W_{1/3})O_3$ (PFW) and ferroelectric $PbTiO_3$ (PT), $(1-x)$PFW–xPT, was synthesized by a *B*-site precursor method and characterized by X-ray diffraction, differential scanning calorimetry, and dielectric measurements. A phase diagram between PFW and PT has been established. The diffuse phase transition temperature ($T_{max} \approx 180$ K) of PFW was found to continuously increase with the increasing amount of Ti^{4+} ions on the *B*-site. At the same time, the relaxor ferroelectric behavior of PFW is gradually transformed toward a normal ferroelectric state, as evidenced by sharp and nondispersive peaks of dielectric permittivity around T_C for $x \geq 0.25$. At room temperature, a transition from a cubic to a tetragonal phase takes place with x increased up to 0.25. A morphotropic phase boundary is located within the composition interval $0.25 \leq x \leq 0.35$, which separates a pseudocubic (rhombohedral) phase from a tetragonal phase.

Key Words: **complex perovskite; $Pb(Fe_{2/3}W_{1/3})O_3$–$PbTiO_3$; relaxor ferroelectricity; dielectric properties; phase diagram; morphotropic phase boundary; phase transitions.**

1. INTRODUCTION

Complex perovskite $Pb(Fe_{2/3}W_{1/3})O_3$ (PFW) exhibits a broad and diffused maximum of dielectric permittivity around $T_{max} = 180$ K with a strong frequency dispersion (1). Macroscopically, no ferroelectric phase transition occurs upon cooling through T_{max}. These properties are characteristic of relaxor ferroelectric behavior (2–4). PFW shows an average primitive cubic perovskite structure with $Pm\bar{3}m$ group, in which the *A*-sites are occupied by Pb^{2+} ions and the octahedral *B*-site positions are filled by Fe^{3+} and W^{6+} ions at random. On the microscopic scale, polar nanoregions (or clusters) are expected to exist due to composition fluctuations and partial order/disorder, which is believed to be the origin of the relaxor ferroelectric behavior (2–4). On the other hand, PFW contains paramagnetic Fe^{3+} ($3d^5$) ions on the *B*-site with an occupancy of 66.7%. Magnetic ordering may occur upon cooling while the polar microdomains develop. PFW single crystals indeed show two antiferromagnetic orderings at $T_{N1} = 350$ K and $T_{N2} = 20$ K, respectively (5). The former was supposed to result from the magnetic interactions *via* the superexchange pathway, $-Fe^{3+}-O-Fe^{3+}-$, within the disordered local clusters, and the latter would arise from the $-Fe^{3+}-O-W-O-Fe^{3+}-$ superexchange pathway within the ordered microdomains (5). The magnetic and dipolar interactions in PFW are expected to give rise to some peculiar properties in this relaxor.

It was known that the synthesis of pure PFW is difficult because of the formation of other nonferroelectric phases, such as pyrochlore, $PbWO_4$, and Pb_2WO_5. Almost-pure polycrystalline PFW was prepared using the columbite/wolframite precursor method (6), with improved dielectric properties compared with the samples prepared by the conventional mixed-oxide method (7, 8), in which lead tungsten oxide second phases ($PbWO_4$ and Pb_2WO_5) seemed to be present in a remarkable amount. In the columbite process, direct reaction between the *B*-site metal oxides and PbO is basically prohibited at the early stage, preventing the formation of the pyrochlore-type phase.

When PFW forms multicomponent systems with other ferroelectrics, the materials exhibit excellent multifunctional properties due to an improvement of dielectric properties, a higher Curie temperature, and a lower firing temperature (9–11). Therefore, PFW has been known as a promising material for a multilayered ceramic capacitor (11). Among the binary systems, $Pb(Fe_{2/3}W_{1/3})O_3$–$PbTiO_3$ (PFW–PT) is of particular interest. PFW is a relaxor ferroelectric and antiferromagnet, while $PbTiO_3$ is a typical ferroelectric with a sharp maximum of dielectric constant at $T_C = 763$ K. It is possible to move the Curie temperature to around room temperature and to modify the relaxation behavior by choosing an appropriate amount of PT in the system. Some results were reported on the preparation of PFW and PFW–PT at high temperatures using additives and an

[1]To whom correspondence should be addressed. Fax: (604) 291-3765. E-mail: zye@sfu.ca.

0022-4596/02 $35.00

excess amount of PbO (9). But systematic studies of the PFW–PT system in terms of phase transitions and dielectric and magnetic properties are still lacking.

In the present work, an improved *B*-site precursor method is developed to synthesize a highly pure perovskite phase of $(1-x)$PFW–xPT. The phase formation and the structural parameters are characterized by X-ray diffraction. Phase transitions and the related properties are studied by differential scanning calorimetry and dielectric measurements. The phase relationship is established by a phase diagram.

2. SYNTHESIS BY A *B*-SITE PRECURSOR METHOD

A modified *B*-site precursor method (12–15) was adopted for the synthesis of $(1-x)$PFW–xPT with various compositions, $x = 0$, 0.10, 0.20, 0.25, 0.30, 0.325, 0.35, 0.40, 0.60, and 0.80. It consists of a two-step reaction process taking place consequently. In the first step, an intermediate (or precursor) phase or a mixture of phases was formed by reacting the oxides of the *B*-site elements. In the second step, the *B*-site precursor phase was reacted with the other (*A*-site) reactants to form the complex perovskite phase. When the intermediate phase has a columbite structure, such as $MgNb_2O_6$, the *B*-site precursor method can be referred to the so-called "columbite method" (12).

Fe_2O_3 (99.99%, Alfa) and WO_3 (99.8%, Alfa) were first finely ground in acetone media for 4 h, and then dried and preheated at 1000°C for 2 h to form Fe_2WO_6. Afterward, PbO (99.99%, GFS Chemicals) or a mixture of PbO and TiO_2 (99.99%, Aldrich) was mixed with Fe_2WO_6 in a stoichiometric ratio and finely ground in acetone media for 4 h. The mixture was initially calcined at 800°C for 2 h, reground, and finally sintered at 850°C–890°C for 2–3 h. With the increase of PT component, the sintering temperature was increased slightly. The temperature ramps were controlled at 5°C/min for heating and 2°C/min for cooling. PFW and PFW–PT were formed according to the following solid state reactions:

$$Fe_2WO_6 + 3PbO \rightarrow 3Pb(Fe_{2/3}W_{1/3})O_3 \qquad [1]$$

$$(1-x)Fe_2WO_6 + 3xTiO_2 + 3PbO \rightarrow 3Pb[(Fe_{2/3}W_{1/3})_{1-x}Ti_x]O_3. \qquad [2]$$

By the *B*-site precursor method, the Fe_2WO_6 phase was presynthesized with a structure resembling the perovskite one, and direct reactions between PbO and WO_3 were avoided. Therefore, subsequent formation of the pyrochlore structure has been suppressed. Compositional analysis performed by EDX on electromicroscopy confirmed the homogeneity and the stoichiometry for all the compositions. In addition, the temperature of the maximum dielectric constant (T_m or $T_C = 178$ K at 1 kHz) of PFW prepared by the precursor method is identical to that of PFW single crystals, indicating that no compositional errors were introduced.

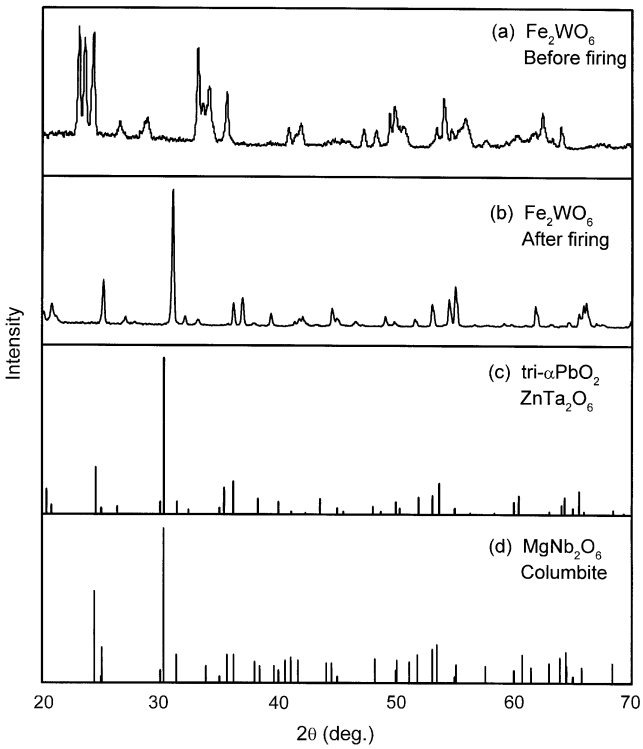

FIG. 1. X-ray diffraction patterns of (a) Fe_2WO_6 before firing; (b) Fe_2WO_6 after firing at 1000°C for 2 h; (c) $ZnTa_2O_6$ of tri-αPbO_2 structure (16); and (d) $MgNb_2O_6$ of columbite structure (17).

3. PHASE ANALYSIS AND STRUCTURAL REFINEMENT

Phase analysis and structural refinement of the $(1-x)$PFW–xPT system were performed based on powder X-ray diffractograms (Cu$K\alpha$ radiation, $\lambda = 1.5418$ Å). Figure 1 shows the XRD patterns of Fe_2WO_6 before and after calcining, as well as the diffraction spectra of $ZnTa_2O_6$ (tri-αPbO_2 structure) (16) and $MgNb_2O_6$ (columbite structure) (17) as references. From the comparison of Fig. 1b with Fig. 1c, it can be seen that Fe_2WO_6, obtained as the *B*-site precursor compound $B'_2B''O_6$, crystallizes in a tri-αPbO_2-type structure, rather than in a columbite-type structure as reported in Ref. (6). The two structures, which resemble the perovskite one, can be distinguished from each other according to the XRD patterns given in Figs. 1c and 1d.

Identification and analysis of the perovskite phase with regard to the undesirable pyrochlore phase was carried out after each reaction step. The content of pyrochlore phase

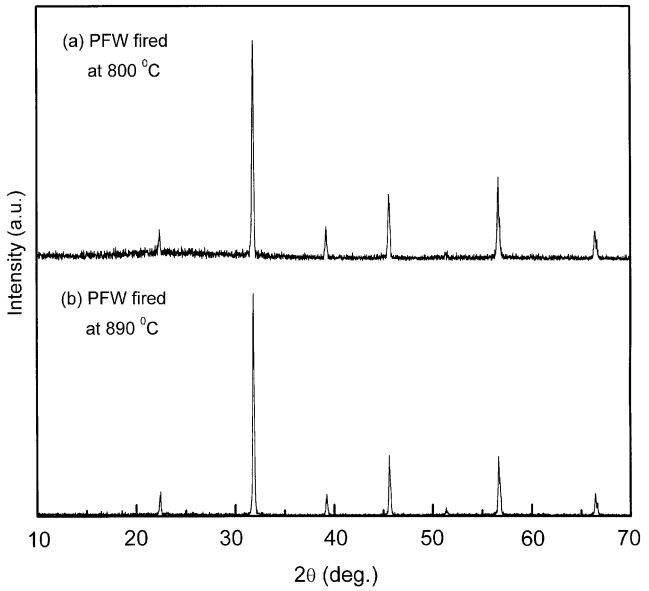

FIG. 2. X-ray diffraction patterns of (a) $Pb(Fe_{2/3}W_{1/3})O_3$ powder after calcining at 800°C and (b) PFW ceramics after sintering at 890°C, both showing a perovskite phase of PFW.

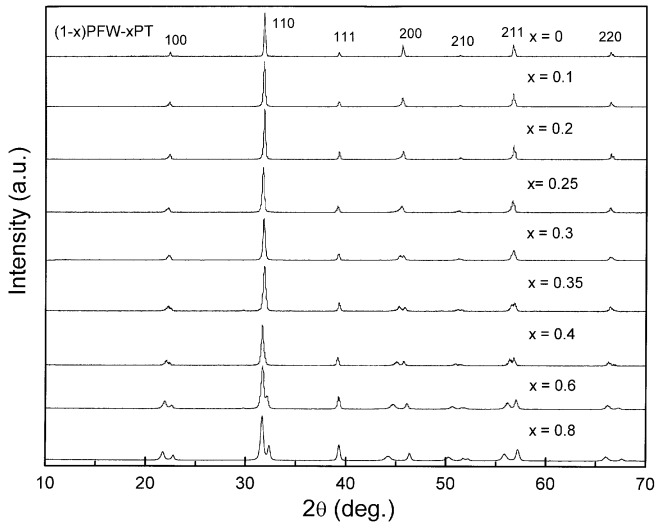

FIG. 3. X-ray diffractograms for various compositions of the $(1-x)$PFW–xPT system at room temperature, showing a tetragonal splitting for $x \geq 0.25$.

in the products was calculated according to the following equation (18),

$$\text{pyrochlore content (\%)} = \{I_{\text{pyro}}(222)/[I_{\text{pyro}}(222) + I_{\text{perov}}(110)]\} \times 100, \quad [3]$$

where $I_{\text{pyro}}(222)$ is the intensity of the (222) reflection peak of the pyrochlore phase and $I_{\text{perov}}(110)$ is the intensity of the (110) peak of the perovskite phase. Figure 2 shows the XRD patterns of the PFW samples prepared at 800°C for 2 h (a) and sintered at 890°C (b). A nearly pure PFW phase was formed after calcination (with the pyrochlore content below the detectable limit) and a highly pure PFW product was obtained after sintering. These results show an improvement in the preparation of pure PFW by the *B*-site precursor technique, compared with the conventional mixed-oxide method (10, 19, 20).

The XRD patterns of various composition of $(1-x)$PFW–xPT ($x = 0$ to 0.8) are presented in Fig. 3. The compounds of $0 \leq x \leq 0.25$ show a cubic perovskite structure at room temperature. When PT content x is increased higher than 0.25, the diffraction peaks (100), (200), and (211) start splitting. With further increase of x, the splitting becomes more and more significant for all the indexed peaks except for (111), indicating that $(1-x)$PFW–xPT gradually transforms from a pseudocubic perovskite structure into a tetragonal structure.

The lattice parameters of $(1-x)$PFW–xPT were refined in the cubic $Pm\bar{3}m$ and/or tetragonal $P4mm$ phase. Figure 4 shows the variation of the lattice parameters as a function of PT content. The parameter a of the cubic perovskite phase decreases slightly from 3.9909 Å to 3.9734 Å with the increase of x from 0 to 0.2. Such a variation can be attributed to the substitution of the smaller Ti^{4+} ions ($r = 0.605$ Å) for the Fe^{3+} ions ($r = 0.645$ Å) on the *B*-site, while W^{6+}

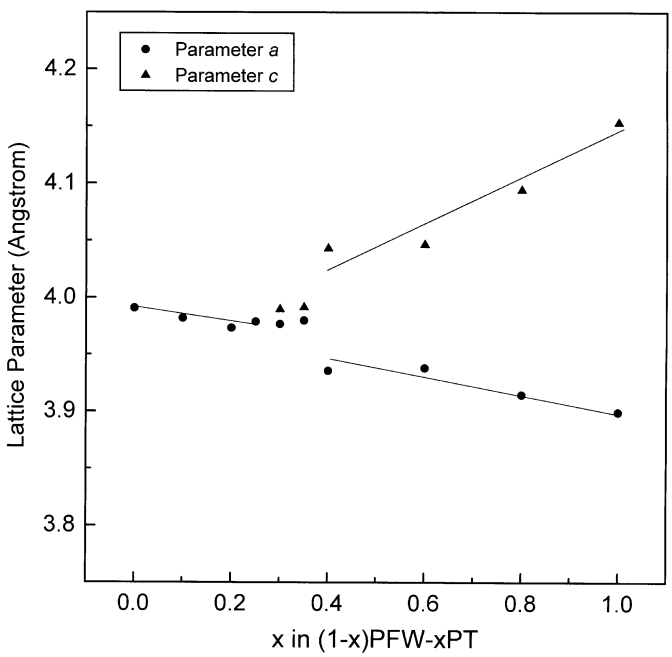

FIG. 4. Variation of the pseudocubic (*a*) and tetragonal (*a* and *c*) lattice parameters at room temperature as a function of x for $(1-x)$PFW–xPT. Solid lines are a guide for the eye.

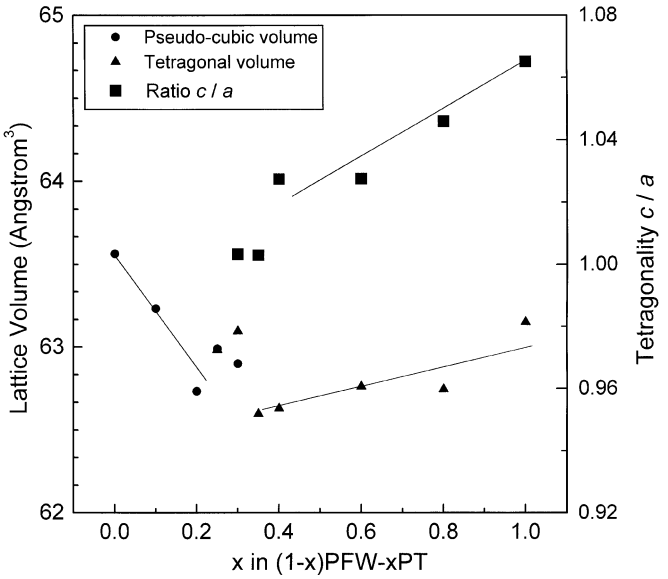

FIG. 5. Variation of the pseudocubic and tetragonal unit cell volume and the tetragonality c/a as a function of Ti content in $(1-x)$PFW–xPT. Solid lines are a guide for the eye.

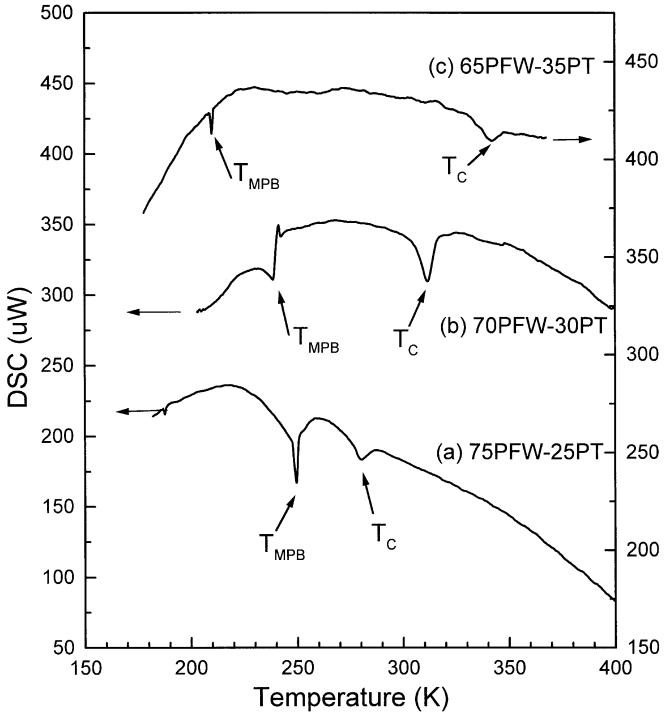

FIG. 6. DSC scanning curves upon heating for (a) 0.75PFW–0.25PT, (b) 0.70PFW–0.30PT, and (c) 0.65PFW–0.35PT.

($r \approx 0.60$ Å) has almost the same size as Ti^{4+} (21). At $x = 0.4$, the tetragonal symmetry can be monitored with a clear split of the parameters, $a = 3.9357$ Å and $c = 4.0433$ Å. With further increase of x from 0.4 to 1.0, a continues to decrease slightly while c increases more pronouncedly. Accordingly, the c/a ratio augments from 1.0273 (for $x = 0.4$) to 1.0651 (for $x = 1.0$), indicating an increase of tetragonality (Fig. 5). The compositions of $x = 0.30$–0.35 show a very small split between a and c, and a c/a ratio close to 1, indicating the onset of the tetragonal distortion from the cubic symmetry.

The corresponding volume change *versus* PT content is also presented in Fig. 5. The volume of the cubic phase decreases from 63.5637 Å^3 to 62.7338 Å^3 with x rising from 0 to 0.2. The volume of the tetragonal phase increases slightly from 62.5969 Å^3 (for $x = 0.4$) to 63.1500 Å^3 (for $x = 1.0$), suggesting that the size effect of Ti^{4+} ions is predominated by the tetragonal distortion of the unit cell. For $x = 0.25$ to 0.35, an irregular variation of lattice volume is observed, suggesting that both the cubic and the tetragonal phases may coexist within that composition range at room temperature.

4. DIFFERENTIAL SCANNING CALORIMETRY

Differential scanning calorimetry (DSC) was carried out to analyze the phase transitions in the $(1-x)$PFW–xPT system, in which a morphotropic phase boundary (MPB) is expected. The analysis was performed using a Seiko ExStar DSC 6200 apparatus. All the DSC runs were performed under flowing nitrogen gas using alumina as reference. The samples were first heated quickly to about 600 K to eliminate any adsorbed H_2O traces, and then cooled to 170 K, followed by heating to 500 K at a heating/cooling rate of 10°C/min.

Figure 6 shows some DSC results. Upon heating, two endothermic peaks occur at 250 and 281 K, 240 and 311 K, and 210 and 342 K, respectively, for each of the compositions $x = 0.25$, 0.30, and 0.35. The low-temperature thermal event indicates the morphotropic transition from the low-temperature phase to the tetragonal phase at T_{MPB}, and the high-temperature peak shows the tetragonal to cubic phase transition at T_C. Therefore, the morphotropic phase boundary of the $(1-x)$PFW–xPT system is localized in the composition range $0.25 \leq x \leq 0.35$.

5. DIELECTRIC MEASUREMENTS

The complex dielectric permittivity of $(1-x)$PFW–xPT ceramics was measured as a function of temperature at frequencies $f = 1$, 10, and 100 kHz under isothermal conditions. The measurements were carried out upon heating from 100 to 600 K by means of a computer-controlled impedance analyzer (Solartron 1260) associated with a dielectric interface (Solartron 1296).

The temperature and frequency dependences of the real part of dielectric permittivity are presented in Fig. 7 for different compositions. In Fig. 7a, 0.90PFW–0.10PT

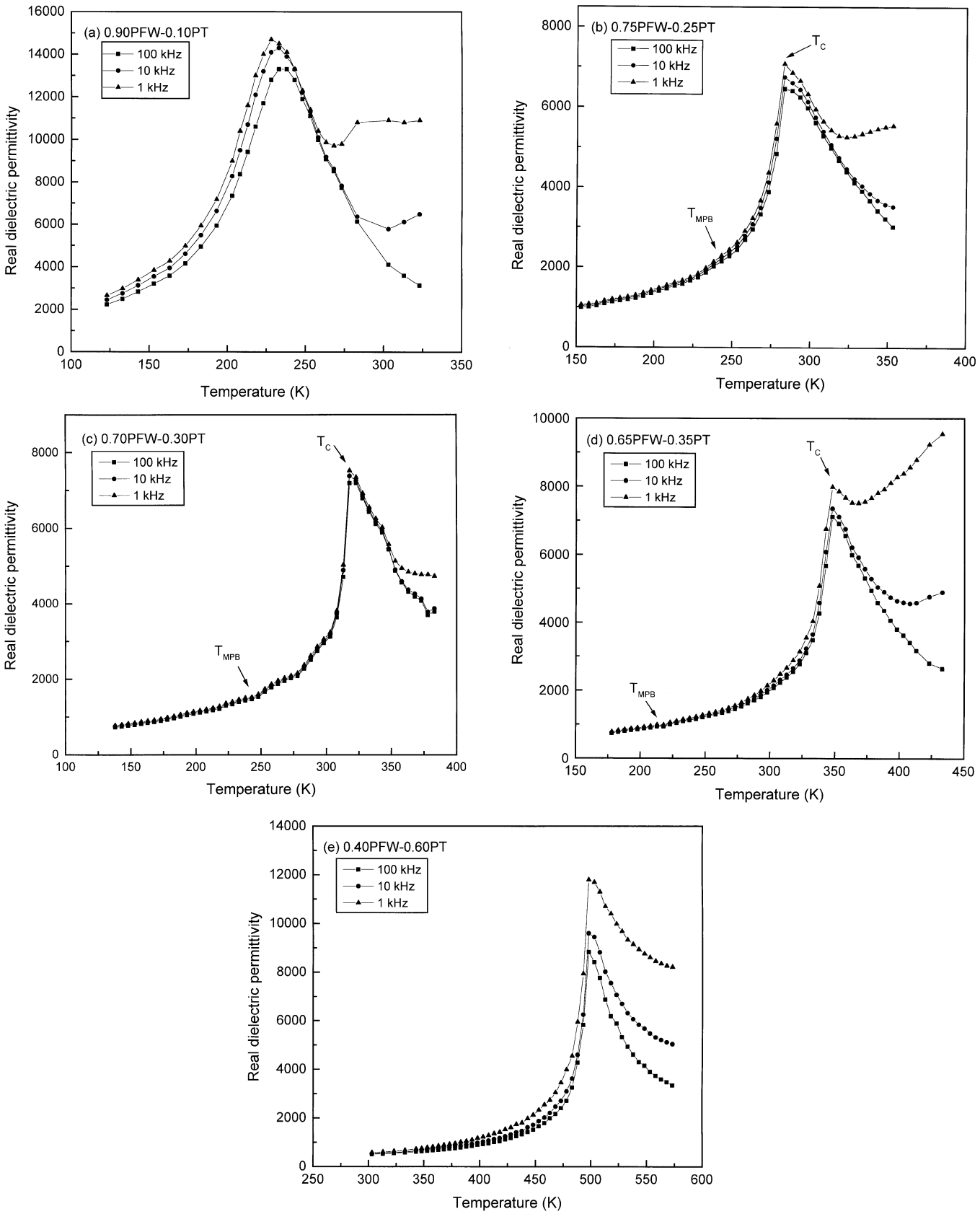

FIG. 7. Temperature dependences of the real part of dielectric permittivity (ε'_r) at frequencies $f = 1$, 10, and 100 kHz for various compositions: (a) 0.90PFW–0.10PT; (b) 0.75PFW–0.25PT; (c) 0.70PFW–0.30PT; (d) 0.65PFW–0.35PT; and (e) 0.40PFW–0.60PT.

exhibits a broad maximum of dielectric constant with strong frequency dispersion, which is reminiscent of the relaxor ferroelectric behavior of PFW crystal (1). The temperature of the permittivity maximum T_{max} (or T_C) varies from 228 K at 1 kHz to 236 K at 100 kHz. The maximum value of the dielectric constant decreases with increasing frequency. The dielectric dispersion below T_C reflects typical relaxor ferroelectric behavior arising from the responses of polar microdomains (relaxators) with a spectrum of relaxation time (2–4). Since the relaxation appears at low temperature ($T < 225$ K), the contribution of mobile changes is not significant. In the high-temperature paraelectric phase ($T > T_C$), another frequency dispersion appears, which is particularly significant at low frequencies. Such low-frequency dispersion (LFD) can be attributed to the conductivity effects due to slowly mobile electronic charges. These charges arise from the Fe^{3+} ions (d^5), which are usually combined with Fe^{2+} ions to form charge defects. Electron hopping between Fe^{3+}/Fe^{2+} ions would result in the conductivity, which in turn will give rise to dielectric dispersion, more remarkable at lower frequencies, as shown in Fig. 7a. The LFD was also observed in other relaxor ferroelectric systems, such as $Pb(Mg_{1/3}Nb_{2/3})O_3$–$PbTiO_3$, where the contribution to the electronic conduction comes from structural defects (3). The reason the LFD is more significant in the high-temperature phase is two-fold. First, the paraelectric phase of PFW–PT has a disordered cubic perovskite structure like PFW (5), with the Fe^{3+}, W^{6+}, and Ti^{4+} ions statistically distributed on the *B*-sites. This provides a relatively short Fe^{3+}–Fe^{3+} distance, favoring the electron hopping between the ferric ions. Second, the LFD appears more significantly in the high-temperature range (> 275 K), where thermal activation enhances the electric conduction and hence the low-frequency dispersion. A detailed impedance spectroscopic study is underway to quantitatively analyze the contributions of different electrically active parts.

With PT content increased to 20%, the low-temperature dielectric dispersion (i.e., the relaxor relaxation below T_C) is significantly attenuated. At the same time, T_C increases to about 275 K. The dielectric properties of 0.75PFW–0.25PT are shown in Fig. 7b, where no significant relaxation appears around and below $T_C = 288$ K, indicating that the substitution of Ti^{4+} for $(Fe_{2/3}W_{1/3})^{4+}$ has induced a transformation from the relaxor regime in PFW toward a long-range (normal) ferroelectric state. The dielectric permittivity of 0.70PFW–0.30PT shows nondispersive peaks at $T_C = 320$ K, corresponding to the ferro- to paraelectric phase transition (Fig. 7c). T_C further increases to 250 K and 500 K for $x = 0.35$ (Fig. 7d) and 0.60 (Fig. 7e), respectively.

For the compositions around the morphotropic phase boundary, $x = 0.25$–0.35, in contrast to the DSC measurements in which the morphotropic phase transition has been clearly detected with T_{MPB} varying from 250 K to 210 K, the temperature dependences of dielectric constant (Fig. 7b–7d) show only weak or broad anomalies around T_{MPB}. This phenomenon can be understood on the basis of the fact that the MPB transition occurs between two polar (and ferroelectric) phases, and therefore involves relatively weak structural instability and small net polarization changes compared with the ferro-/paraelectric transition at T_C. As a result, the dielectric measurements usually show weak effects for the MPB transition. This behavior was also observed in the other relaxor-based solid solution systems with MPB, such as $Pb(Mg_{1/3}Nb_{2/3})O_3$–$PbTiO_3$ (22) and $Pb(Zn_{1/3}Nb_{2/3})O_3$–$PbTiO_3$ (23), in which the MPB transition appears as a weak and broad dielectric anomaly, while it can be clearly detected as a first-order transition either by optical domain studies (24) or by DSC measurements (with appearance of latent heat) (25). Therefore, thermal analysis by DSC is more reliable for detecting the morphotropic phase transition in the PFW–PT system.

6. PHASE DIAGRAM OF $Pb(Fe_{2/3}W_{1/3})O_3$–$PbTiO_3$

Based on the results of XRD, DSC, and dielectric measurements, a phase diagram for the $(1 - x)$PFW–xPT system has been established, as shown in Fig. 8. It indicates the phase boundaries and phase transition temperatures of

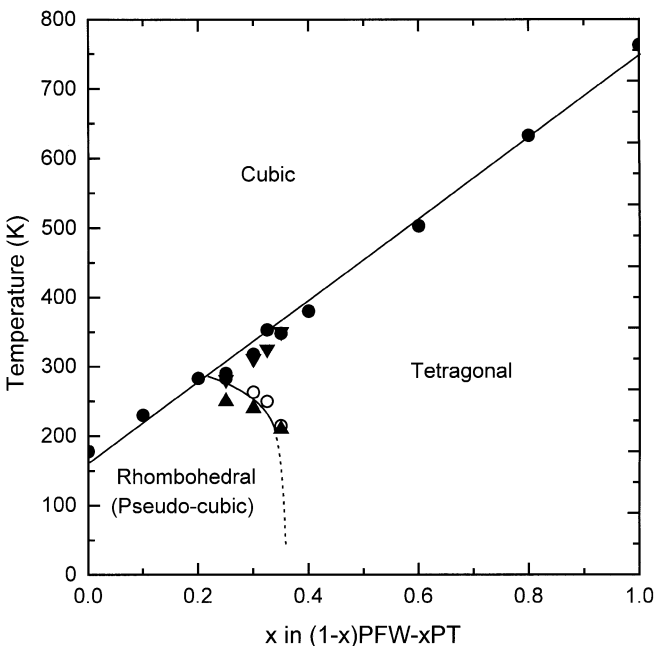

FIG. 8. Phase diagram of the $(1 - x)$PFW–xPT system delimiting the high-temperature cubic phase and the low-temperature ferroelectric rhombohedral (pseudocubic) and tetragonal phases. A morphotropic phase boundary (MPB) is located at $0.25 \leq x \leq 0.35$. Up and down triangles represent the transition temperatures measured by DSC analysis; filled and open circles correspond to the phase transition temperatures detected by dielectric measurements.

the solid solution system. The up and down triangles represent the transition temperatures detected by DSC analysis and the filled and open circles correspond to the phase transition temperatures obtained from the dielectric measurements. The Curie temperature increases almost linearly with the increase of PT content x, from $T_{max} = 178$ K for PFW to $T_C = 763$ K for PT. The symmetry of the low-temperature ferroelectric phase with a small PT content can be refined in a pseudocubic symmetry with a slight rhombohedral $R3m$ distortion, as in the case of $Pb(Zn_{1/3}Nb_{2/3})O_3$–PT (26) and $Pb(Mg_{1/3}Nb_{2/3})O_3$–PT (27) systems. A cubic perovskite structure appears above the Curie temperature line. At room temperature, the cubic phase transforms into the tetragonal phase at a PT content of about 25%. The cubic and tetragonal phases coexist for the compositions around the phase boundary, as shown by the anomalies in the variations of lattice parameters and volume (Figs. 4 and 5). Below the T_C line, the ferroelectric rhombohedral and tetragonal phases are separated by a morphotropic phase boundary (MPB) which is located in the composition range $0.25 \leq x \leq 0.35$ below 280 K. At the compositions near the MPB, both the rhombohedral and the tetragonal phases may coexist. For compositions close to the MPB, successive phase transitions from the rhombohedral to the tetragonal and then to the cubic phase may occur upon heating, as revealed by the DSC analysis (Fig. 6).

7. CONCLUSIONS

A B-site precursor method, which consists of forming the tri-αPbO_2-type Fe_2WO_6 phase prior to final reactions with PbO or $(PbO + TiO_2)$, has been developed to prepare a pure and complete solid solution system of $(1-x)Pb(Fe_{2/3}W_{1/3})O_3$–$xPbTiO_3$. The structural refinements based on X-ray diffractograms at room temperature indicate that the perovskite $(1-x)$PFW–xPT transforms from a cubic phase to a tetragonal phase at a PT content of $x \geq 0.25$, with a splitting of the cubic lattice parameter a into the tetragonal parameters a and c.

The temperature dependences of the dielectric permittivity at various frequencies have revealed that the ferroelectric phase transition temperature T_C increases with the increasing Ti^{4+} content on the B-site, while the relaxor ferroelectric behavior of PFW is gradually transformed into a normal (long-range) ferroelectric state, as evidenced by the sharp and nondispersive dielectric permittivity peaks around T_C for $x \geq 0.25$. For compositions $0.25 \leq x \leq 0.35$, the DSC analyses have revealed a low-temperature phase transition at T_{MPB} which is related to the existence of a morphotropic phase boundary, in addition to the high-temperature ferro-/paraelectric phase transition at T_C.

A complete phase diagram for the $(1-x)$PFW–xPT system has been established, which delimits a high-temperature paraelectric cubic phase, a ferroelectric rhombohedral (pseudocubic) phase, and a ferroelectric tetragonal ($P4mm$) phase. The morphotropic phase boundary is located at $0.25 \leq x \leq 0.35$, which separates the rhombohedral phase from the tetragonal phase. PFW–PT compositions within the PMB range exhibit successive phase transitions from the rhombohedral to the tetragonal and to the cubic phase upon heating. Such a phase diagram is of relevance to further investigation and understanding of the magnetic, dielectric, and magnetoelectric properties of the PFW–PT system.

ACKNOWLEDGMENTS

The authors thank Drs. M. Dong and M. Mahesh-Kumar for technical help. This work was supported by the Natural Science and Engineering Research Council of Canada (NSERC).

REFERENCES

1. Z.-G. Ye and H. Schmid, *Ferroelectrics* **162,** 119 (1994).
2. L. E. Cross, *Ferroelectrics* **76,** 241 (1987).
3. L. E. Cross, *Ferroelectrics* **151,** 305 (1994).
4. Z.-G. Ye, *Key Eng. Mater.* **155–156,** 81 (1998).
5. Z.-G. Ye, K. Toda, M. Sato, E. Kita, and H. Schmid, *J. Korean Phys. Soc.* **32,** S1028–S1031 (1998).
6. L. Zhou, P. M. Vilarinho, and J. L. Baptista, *J. Mater. Sci.* **33,** 2673–2677 (1998).
7. P. M. Vilarinho and J. L. Baptista, *J. Eur. Ceram. Soc.* **11,** 407 (1993).
8. C. H. Lu, N. Ishizawa, K. Shinozaki, N. Mizutani, and M. Kato, *J. Mater. Sci. Lett.* **7,** 1078 (1988).
9. Y.-J. Kim and S.-W. Choi, *Ferroelectrics* **186,** 287–292 (1996).
10. M. Yonezawa, *Am. Ceram. Soc. Bull.* **62,** 1375 (1983).
11. T. R. Shrout and A. Halliyal, *Am. Ceram. Soc. Bull.* **66,** 704 (1987).
12. S. L. Swartz and T. R. Shrout, *Mater. Res. Bull.* **17,** 1245 (1982).
13. A. Halliyal, U. Kumar, R. E. Newhnam, and L. Cross, *Am. Ceram. Soc. Bull.* **66,** 671 (1987).
14. B.-H. Lee, N.-K. Kim, J.-J. Kim, and S.-H. Cho, *Ferroelectrics* **211,** 233 (1998).
15. M.-C. Chae, S.-M. Lim, and N. K. Kim, *Ferroelectrics* **242,** 25 (2000).
16. Wong-Ng, H. McMurdie, B. Paretzkin, C. Hubbard, and A. Dragoo, JCPDS–ICDD File #39-1484 [*Powder Diffraction* **3,** 121 (1998)].
17. C. Roob and McCarthy, JCPDS–ICDD File #33-875.
18. G. Drazic, M. Trontelj, and D. Kolar, *Mater. Sci. Eng. B* **26,** 189–196 (1994).
19. G. A. Smolenskii, A. I. Agranovskaya, and V. A. Isupov, *Sov. Phys. Solid State* **1,** 907 (1959).
20. M. Yonezawa and T. Ohno, "Proceedings of the Japan–US Study Seminar on Dielectric and Piezoelectric Ceramics," **T-8,** pp. 1–4, 1982.
21. R. D. Shannon, *Acta. Crystallogr. A* **32,** 751 (1976).
22. S. W. Choi, T. R. Shrout, S. J. Jang, and A. S. Bhalla, *Mater. Lett.* **8,** 253 (1989).
23. L. Zhang, M. Dong, and Z.-G. Ye, *Mater. Sci. Eng. B* **78,** 96 (2000).
24. Z.-G. Ye and M. Dong, *J. Appl. Phys.* **87,** 2312 (2000).
25. M. Mendoza and Z.-G. Ye, unpublished.
26. J. Kuwata, K. Uchino, and S. Nomura, *Jpn. J. Appl. Phys.* **21,** 1298 (1982).
27. T. R. Shrout, Z. P. Chang, N. Kim, and S. Markgraf, *Ferroelectrics Lett.* **12,** 63 (1990).